Chapter

Spatial Terahertz-Light Modulators for Single-Pixel Cameras

Rayko Ivanov Stantchev and Emma Pickwell-MacPherson

Abstract

Terahertz imaging looks set to become an integral part of future applications from semiconductor quality control to medical diagnosis. This will only become a reality when the technology is sufficiently cheap and capabilities adequate to compete with others. Single-pixel cameras use a spatial light modulator and a detector with no spatial-resolution in their imaging process. The spatial-modulator is key as it imparts a series of encoding masks on the beam and the detector measures the dot product of each mask and the object, thereby allowing computers to recover an image via post-processing. They are inherently slower than parallel-pixel imaging arrays although they are more robust and cheaper, hence are highly applicable to the terahertz regime. This chapter dedicates itself to terahertz single-pixel cameras; their current implementations, future directions and how they compare to other terahertz imaging techniques. We start by outlining the competing imaging techniques, then we discuss the theory behind single-pixel imaging; the main section shows the methods of spatially modulating a terahertz beam; and finally there is a discussion about the future limits of such cameras and the concluding remarks express the authors' vision for the future of single-pixel THz cameras.

Keywords: spatial light modulator, single pixel camera, compressed sensing, Hadamard imaging, terahertz time-domain spectrometer, single-element detectors, sub-wavelength resolution

1. Introduction

Visual information from the eyes generates vast amounts of data for the human brain to process, and provides us with unparalleled clarity and insight into the world we live in. Imaging with terahertz (THz) radiation is a research field that has gained a lot of interest and is in the process of moving from research laboratories to commercial applications [1–4]. As such, the THz research field has grown so much that it has become impossible for a single human to be able to keep track of all developments [4]. Nevertheless, it is possible to outline why there is great interest and potential in THz imaging technology. Most non-conductive materials and non-polar liquids are THz transparent, useful for non-invasive inspection of many multi-component or buried systems, such as paintings [5], electronic circuits [6], space shuttle panels [7] and carbon-fiber composites [8]. Other possibilities are the measurement of picosecond processes in semiconductors [9], quality control of

pharmaceutical tablets [10] and non-invasive detection of explosive substances [11]. A plethora of fundamental material resonances, such as phonons, rotations of molecules and precessions of spins, are observable and controllable by THz radiation [12]. Bio-medical applications are highly alluring most notably because the THz photon energies are non-ionizing and high-water sensitivity gives rise to label-free diagnosis of diseases that alter water content, such as cancer [13] and diabetic foot syndrome [14]. There is also the possibility of damaging or repairing DNA with intense THz radiation [15].

With so many possible applications, the reason why THz radiation is barely used outside of laboratories is due to costs of current THz technology. In particular to imaging, the technology is either too expensive, too slow or sacrifices some detection capability (such as picosecond temporal resolution). This is because materials which are suitable for efficient THz detection simply do not exist. This has resulted in THz detector arrays normally working in either narrowbands [16] or needing cryogenic temperatures for sensitive detection [17]. However, microbolometer arrays have very large bandwidths at room temperature operation [18] and when combined with digital holography they can measure both the amplitude and phase of THz radiation [19, 20]. Unfortunately bolometers achieve frequency resolution with a frequency selective source and they do not offer picosecond temporal resolution. This is acceptable for some applications such as detecting concealed weapons, however for applications where time gated detection is used, for example in extracting depths of painting coatings in original art works [5], it becomes unfeasible. An another imaging technique is to project a THz image on an electro-optic crystal then use visible light CCD arrays to spatially map-out the THz field incident onto the crystal [21, 22]. This does not sacrifice the temporal resolution offered time-domain THz spectrometers, however this needs a regen-amplified Ti: Sapphire laser which makes the whole system big and expensive and has prevented the widespread adoption of this technology despite its capabilities. These imaging techniques are all far-field, apart from [21], meaning that they fail to see detail below $\sim 500\mu$m due to the THz wavelengths. There are near-field THz imaging techniques [23–29] which vary from placing AFM-tips next to the sample [23–25], to near-field THz-fiber probes [27] and even air-plasma has been used for sub-wavelength imaging [29]. A very impressive achievement is by M. Eisele, et al. [24] where they obtained 10 nm spatial resolution with 50 fs temporal resolution to reveal the time-dependence of photoexcitation in InAs nanowires.

The aforementioned imaging approaches are the standard imaging techniques, relying on a detector array or raster scanning, however there is another alternative. Namely, using a spatially modulated light beam and a single-pixel detector to obtain an image [30]. Approaches based on this technique are commonly called *computational imaging* because a computer is needed to recover the image although *single-pixel imaging* is another common name. The measurements are obtained sequentially as opposed to in parallel, like in detector arrays, hence this technology is usually slower. This can however be offset by the possibility of obtaining an N-pixel image using fewer measurements by employing techniques known as *compressed sensing* [30, 31]. The main advantage to this technology is that the use of a single-pixel detector greatly enhances the robustness of the system as well as reducing the complexity and cost. This is what makes them attractive for uses in THz-imaging: potential for fast imaging without increasing costs whilst being compatible with single-element detectors such as photoconductive antennas that can measure the amplitude and phase of a THz-pulse with 100 fs temporal resolution. In this chapter single-pixel imaging technologies for use with THz radiation are discussed, where in §2 we discuss the mathematical theory, §3 discusses the current state of the spatial light modulators for THz radiation with regards to the latest implementations of

single-pixel THz cameras. §4 discusses where single-pixel THz cameras are likely to have an advantage over other competing THz technologies and the conclusions §5 summarize the whole chapter and ending with the authors' view of the future development of THz single-pixel cameras.

2. Single-pixel imaging theory

Single-pixel imaging theory concerns itself with obtaining an image of a scene using a detector that can only measure the total amplitude emanating from the scene. The simplest idea is to raster scan an aperture across the field-of-view, building the image pixel by pixel. However, as the aperture is made smaller and smaller, the signal reaching our detector is reduced. We could increase the light incident onto our detector and overcome detector-noise by simultaneously scanning more apertures during each measurement, an idea that originates with Yates in 1935 [32]. In **Figure 1(a)** we show the main principle of this idea; we have a light beam that is spatially modulated which propagates through an object and onto a detector with no spatial resolution. It is of the utmost importance that in each measurement we know which apertures were open and which were closed. Without this information we could never reconstruct an image of the object. Each measurement is the dot product of the spatial encoding mask and the transmission function of the object, which is mathematically expressed as

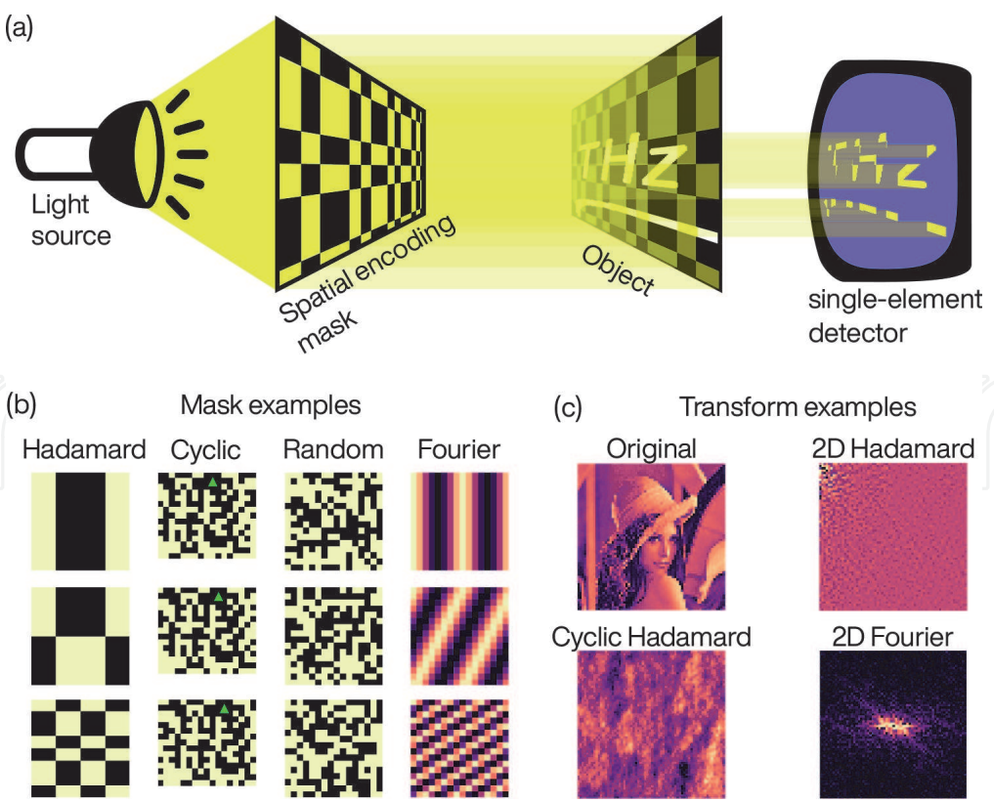

Figure 1.
(a) Imaging with a single-element detector. An encoding mask spatially encodes a beam of radiation, then the beam passes through an object and onto the single-element detector. (b) Spatial encoding masks, where the first, second, third and fourth coloumns were constructed from Sylvester Hadamard, cyclic Hadamard, random and Fourier matrices respectively. The green triangle in the cyclic mask is there as a visual guide. (c) 2D image transform examples. Figure (a) was extracted from reference [33] under creative commons attribution 4.0 international license.

$$y_i = \sum_{j=1}^{N} a_{ij} x_j, \tag{1}$$

where y_i is our i^{th} measurement, a_{ij} holds the spatial information of the i^{th} mask and x_j is the j^{th} pixel of the object. The full set of measurements can be represented by the matrix equation

$$\mathbf{y} = A\mathbf{x}, \tag{2}$$

where the rows of matrix A are shaped into the projected masks (ie. 1D vectors reshaped into 2D masks). Solving Eq. (2) for $\mathbf{x}$ is the cornerstone of single-pixel imaging. In the simpler cases A is an invertible matrix, meaning that $\mathbf{x} = A^{-1}\mathbf{y}$ is sufficient for us to the obtain our image. Alternatively we need to use least squares solvers or complex optimization problems [31], which are commonly used for undersampling procedures where one obtains an image with N pixels using fewer measurements.

A in Eq. (2) is called the basis expansion of our object $\mathbf{x}$. For example, the most commonly know example is if A is the Fourier matrix, then $\mathbf{y}$ is the Fourier transform of our object $\mathbf{x}$. This basis expansion determines the masks that will be projected in each measurement, and in 1(b) we show commonly used spatial encoding masks. Namely, masks constructed from a Sylvester-Hadamard, Cyclic-Hadamard, Random and Fourier matrices. Each one has its own advantages and disadvantages and these are briefly outlined.

The Sylvester-Hadamard matrices are binary, meaning that they are easily implemented, specifically with digital micromirror devices which are relatively cheap and have switch rates upto 20 kHz. The reconstruction technique can also be efficiently calculated by just doing the Fast Hadamard-Walsh transform, meaning one does not need to store A in memory that can be very large (ie. for an $n \times n$ image A would be a $n^2 \times n^2$ matrix). Further, if one implements the 2D transform of the Hadamard-Walsh transform with *sequency* ordering, then it has the effect of concentrating all the coefficients with large amplitudes around the (0, 0) pixel as can be seen in **Figure 1(c)**. This is useful for undersampling procedures with the relevant masks obtained by transforming a series 2D-delta functions [34]. Finally, these are orthogonal matrices meaning they are very robust to detector noise [35]. A side note is that creating such masks at sub-THz wavelength resolutions can create grating diffraction effects as shown in § 5.3.2 of reference [33].

The Cyclic-Hadamard matrices, also known as Paley Type I and type II Hadamard matrices as they were first discovered by Paley in 1933 [36], are orthogonal and circulant matrices made of 1 s and -1 s. This means they have large noise robustness, easy binary implementation and they are constructed by having one vector, $\mathbf{c}$, from which every row is created by cyclic permutations of this vector. For the spatial masks, this means that $i + 1$ mask is obtained by shifting the i mask to left which can be seen in column two of **Figure 1(b)**. This means that these masks are most commonly used as physically manufactured masks and can be placed on spinning discs. These matrices also have a fast-reconstruction technique which based on their circulant nature. Given an equation $\mathbf{y} = C\mathbf{x}$ where is a C is matrix constructed by cyclically shifting the top row $\mathbf{c}$, then we can rewrite it as $\mathbf{y} = \mathbf{c} \circledast \mathbf{x}$ with $\circledast$ being the circular convolution operator. Then by the circular convolution theorem $\mathcal{F}[\mathbf{y}] = \mathcal{F}[\mathbf{c} \circledast \mathbf{x}] = \mathcal{F}[\mathbf{c}]\mathcal{F}[\mathbf{x}]$, where $\mathcal{F}$ is the Fourier transform. This means that $\mathbf{x} = \mathcal{F}^{-1}[\mathcal{F}[\mathbf{y}]/\mathcal{F}[\mathbf{c}]]$, thus if one uses the Fast Fourier Transform then the reconstruction algorithm is very efficient with a complexity of $O(N \log N)$ for an N-pixel image.

Random masks constructed from Bernoulli matrices, or Gaussian random matrices, can also be made from 1 s and -1 s making for easy implementation using binary spatial light modulators. However, these matrices are not directly invertible and using a pseudo-inverse can create stability problems. Therefore convex minimization algorithms are usually used for image reconstruction [30, 31]. The main benefit of this masking approach is that is can be used for undersampling which can greatly reduce the total measurement time at the expense of complicated calculations. References [37, 38] were the first theoretical investigation and one can obtain their reconstruction scripts from reference [39], although reference [40] also freely provides their MATLAB scripts for another minimization algorithm called TVAL3 [41]. These algorithms can be slow, hence a mention needs to be given to reference [42] where Kowarlz et al. creates a pseudo-inverse matrix via Fourier-domain regularization that is able to recover images of quality similar to the slow minimazation algorithms, however with faster calculations based on matrix multiplication methods. Note, they also provide their MATLAB and Python scripts freely on github [43].

Fourier masks are those derived from the Fourier matrix. However, as this is just linear algebra representation of the Fourier transform and we are measuring real images (without imaginary numbers), then we do not need to measure the negative Fourier frequencies as they are just the complex conjugate of their positive frequency counterpart. The Fourier matrix is also orthogonal meaning it has noise robustness equal to the Hadamard matrices as well efficient image reconstruction algorithms, simply the Fast Fourier Transform. These masks, however, are not binary but require grayscale values which limits their deployability. Binary spatial modulators can accomplish this either by temporal dithering, at the expense of slower switch-rates, or by spatial dithering, which creates some quantization errors [34]. Nevertheless, these masks benefit from extensive literature based on the Fourier Transform and various image compression algorithms that can be reversed for image-undersampling procedures.

3. Spatially modulating THz radiation

In this single-pixel imaging modality, the most crucial part is to create a spatially modulated beam. In this respect for the THz regime there are four main methods that can be employed; by creating a physical mechanical mask, by changing the electrical conductivity of a material via the injection/depletion of charge carriers, by controlling the refractive index of liquid crystal cells and by creating a spatially varied beam directly at the THz generation stage.

3.1 Mechanical masks

Creating a physical mask to modulate THz radiation has the great advantage that this is the easiest in terms of manufacturing with great modulation depth, $>99\%$, over very broadband frequency ranges. This is because most semiconductors and plastics are THz transparent whereas conductive metals absorb and reflect THz radiation [44]. Thus PCB manufacturing techniques can be used to create a set of spatial masks. This results in masks that need to be mechanically moved, however if placed on disc high switch-rates could be potentially achieved as discs can spin at high speeds. These techniques were used in references [45, 46].

There is another modulation technique that falls in this mechanical category. Namely, mirror arrays where each mirror can be individually addressed. Such arrays already exist for the visible light regime in the form of digital micromirror

arrays (DMD). However, DMD mirrors are with dimensions around 10 μ m meaning their THz diffraction efficiency is incredibly low. Therefore larger mirrors were manufactured by reference [47]. This means they have good working efficiency and high contrast. **Figure 2** shows their concept in parts (a-c) and their results in parts (d-f). The main problem with these devices is the mirrors have to physically move which creates some limits in regards to the switch rate, otherwise the metallic nature of the mirrors means they have a very broadband modulation frequencies.

3.2 THz modulation by charge carrier injection/depletion

The main principle with this THz modulation technique is based upon the Drude model dielectric function [48, 49].

$$\varepsilon(\omega) = \varepsilon_\infty - \frac{\omega_p^2}{\omega^2 + i\omega/\tau_s}, \tag{3}$$

where τ_s is the carrier scattering time, ε_∞ is frequency independent permittivity due to bound charges, and $\omega_p = \sqrt{Ne^2/m_e\varepsilon_0}$ is the plasma frequency of the material where N is the density of charge carriers with charge e, ε_0 is the vacuum permittivity and m_e is the effective mass. When the incident wave frequency is higher than the

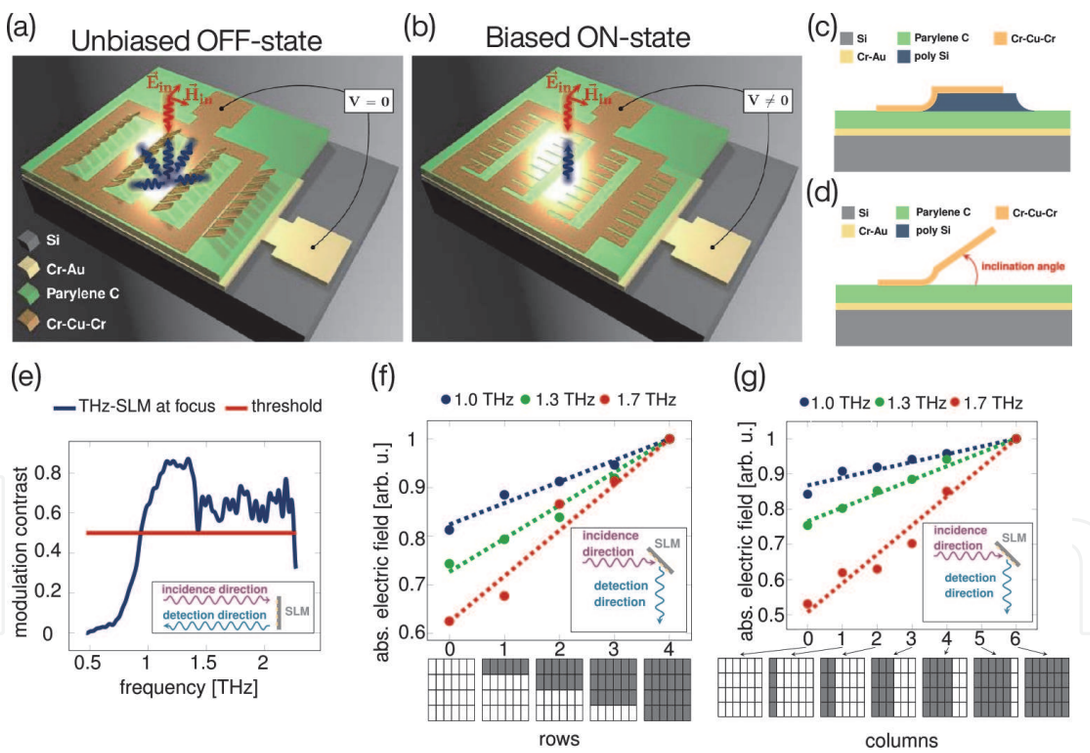

Figure 2.
Schematic of a single pixel of the THz-SLM for normally incident terahertz waves. The pixel is composed of mirrors that are arranged in 4 rows and 8 columns. (a) OFF-state for a bias voltage of 0 V. all mirrors are inclined and incident terahertz radiation (red) is diffracted away (blue) from the transceiver. (b) ON-state for a bias voltage of 37 V. all mirrors are pulled down to the substrate and incident terahertz radiation (red) is reflected (blue) into the transceiver. (c) Schematic cross-sectional view of an unreleased mirror. The base of the mirror adheres to the parylene C, while the part to be released sits on the poly-Si. (d) Schematic cross-sectional view of a released mirror. The base of the mirror adheres to the parylene C, while the released part is inclined due to residual stress in the Cr-Cu-Cr mirror material. (e) Modulation contrast of the THz-SLM. The contrast exceeds a value of 0.5 for a working range from 0.97 THz to 2.28 THz with a maximum contrast of 0.87 at 1.38 THz. (f) Linear dependence of the detected modulated electric field on the number of switched-ON rows in the THz-SLM. (g) Linear dependence of the detected modulated electric field on the number of switched-ON columns in the THz-SLM. Figure reprinted from reference [47] under creative commons attribution 4.0 international license, with figures being relabelled and re-scaled.

plasma frequency, $\omega > \omega_p$, the material has a dielectric response whereas for $\omega < \omega_p$ we have a metallic absorbing material response. Therefore, by controlling N we can change the plasma frequency of the material so the THz wave interacts with a dialectic or a metallic object. This is the main modulation principle of these devices. However, vanadium dioxide (VO_2) needs to be mentioned as it can undergo an insulator-to-metal phase transition via femtosecond optical excitation [50] or an electric field [51]. This material is placed here as using it as a THz modulator has identical experimental implementation, despite the fundamental physics being very different; namely THz modulation via electrical gating or optical excitation.

3.2.1 Optical modulators

Optical based spatial THz-light modulators are currently the best in terms of achieved switch-rate, operational frequency and ease of implementation. Their switch-rate and operational frequencies are both similar to the electrical modulators in that they also rely on modifying the charge carrier density in some material. However, as they use optical light to achieve this, their experimental implementation is very different and due to the current state of visible-light SLMs they are much easier to be implemented. One starts by patterning a visible light beam and then projecting this spatial pattern onto a semiconductor, thereby creating areas that experience large optical excitation and other areas which are left in their ground state. This in turn creates a spatially varying conductivity/absorption profile on the surface of the semiconductor, and thus if a THz beam passes through this surface then the inverse spatial pattern from the visible-light beam is imparted onto the THz beam. The optical excitation can come in two forms, pulsed and continuous wave. For both cases, the carrier concentration is described by

$$N(t) = e^{-t/\tau_l} \int_{-\infty}^{t} G(t') e^{t'/\tau_l} \mathrm{d}t' \tag{4}$$

for carrier generation rate $G(t)$ and excited carrier lifetime τ_l. Reference [52] developed a post-processing technique to account for the above equation, resulting in significantly improving image signal-to-noise when the masks are switched on time-scales comparable to τ_l. However, it should be noted that their mathematical proposal is more general and is able to account for any other physical processes, relevant to the temporal response of the system, that can be described by mathematics.

For continuous wave excitation one needs to consider the photo-carrier generation, recombination and diffusion dynamics within the semiconductor. The steady-state equilibrium carrier concentration within the semiconductor is given by [48].

$$N = \frac{\text{Carrier generation}}{\text{Carrierre combination}} = \frac{2 I_0 T \tau_l}{V \hbar \omega_e}, \tag{5}$$

where I_0 is the incident power per unit area, T is the Fresnel transmittance of the semiconductor, V is the volume where the photocarriers are in, $\hbar\omega_e$ is the photon energy of the photo-excitation beam, and the factor of 2 accounts for the excitation of electrons and holes[1]. The modulation depth is going to be the difference between the ground-state carrier concentration and this new photomodulated concentration. In Eq. (5) it can be seen that large τ_l will give the greatest modulation depth, however this comes at the expense of switch-rate. This is seen in **Figure 3(a)**, where

[1] This assumes that the photogenerated holes and electrons have similar properties such carrier mobility, effective mass, lifetime,... ie. a hole and an electron absorb the same amount of terahertz.

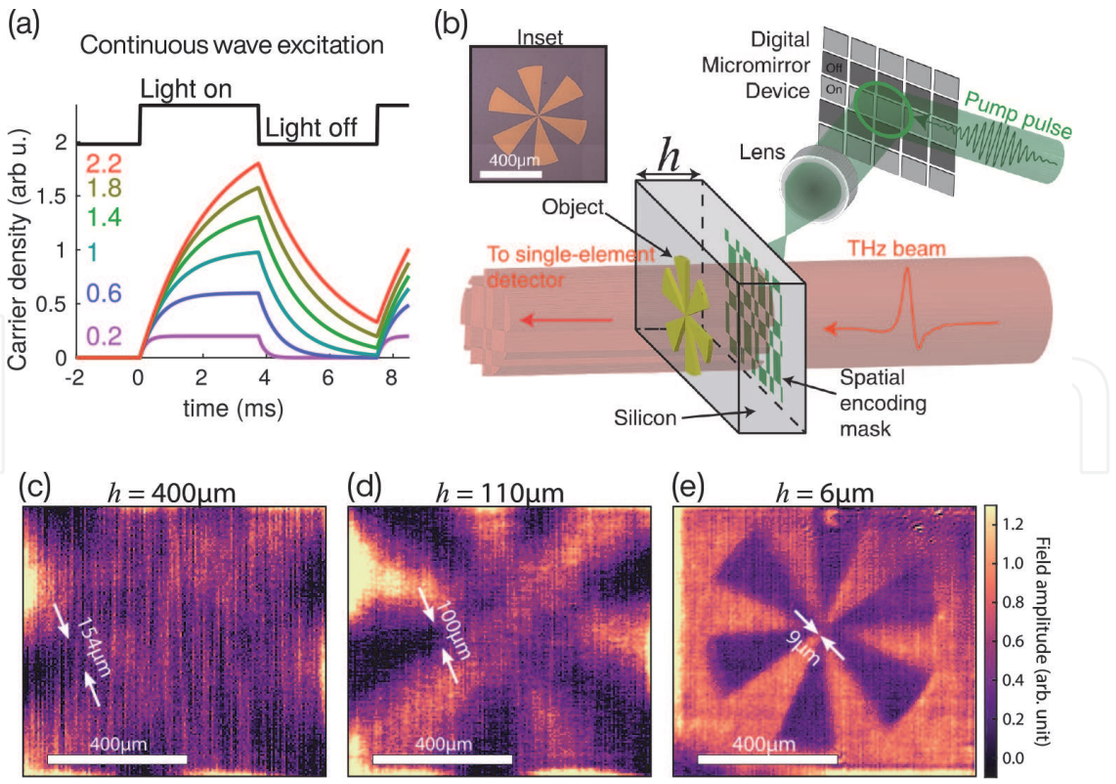

Figure 3.
(a) Carrier density (in arbitrary units) for different carrier lifetimes, shown by the colored numbers in ms, as we switch a continuous wave source on and off. (b) Illustration of imaging setup: Using a digital micromirror device and a lens, a pump pulse is spatially structured and projected onto a silicon wafer. This spatially modulates a coincident THz pulse. This THz pulse then passes through an object and is measured on a single-element THz detector. Inset is an optical image of a resolution test target (cartwheel) manufactured from gold on a 6 μm thick silicon wafer. (c-e) THz images of the cartwheel shown in inset in part (b) taken through 400, 110, 6μm thick silicon wafers respectively. See supplementary fig. S4 for a close-up annotated version of part c. note, the cartwheels in a, b have diameters larger than the field of view. THz polarization is horizontal in experiment figures (b-e) adapted from reference [53]. The Optical Society (OSA) publishing group copyright with re-use permission granted by Rayko I. Stantchev.

we plot the carrier density from Eq. (4) for different carrier lifetimes. It can be seen that for the larger τ_l values the carrier density still has not reached its ground state value of 0, however they reach larger carrier densities hence this will result in larger THz modulation for the same photo-excitation powers. Hooper et al. experimentally studied the excitation powers needed for efficient THz modulation with regards to carrier lifetimes in reference [54]. Further, the physical resolution with which a pattern can imprinted on the THz beam is going to be either limited by the resolution with which we project our visible-light pattern or the carrier diffusion dynamics. In most cases, photomodulators with lifetimes around tens of microseconds are used hence the diffusion lengths are going be hundreds of microns, which is much higher than the limits imposed by the projection of visible light. There is a thorough theoretical study of carrier diffusion and modulation depth for THz spatial light modulators in reference [55].

For pulsed optical-excitation probed by a synchronous THz pulse, Eq. (5) changes because the THz pulse can travel through the spatially photopumped region a few picoseconds after photoexcitation and for $\tau_l > 100ps$ then carrier recombination can be ignored[2] however I_0 then becomes power per pulse per unit area. Further, since the THz pulse can be set to arrive a few picoseconds after

[2] This is also assumes that the pulse repetition period is much longer than the carrier lifetime, ie. the carriers have relaxed back to their ground state by the time the next pulse arrives.

photoexictation, then the carrier diffusion lengths become very small (about 500 nm for silicon [53, 56]). This means that the fundamental resolution is set by the photoexicitation beam provided that one can access the THz near-fields before the THz beam has diffracted due to propagating through space. In practice, this means using ultra-thin photomodulators. **Figure 3(b)** show the setup of a study which shows how the THz image resolution is affected by the photomodulator thickness, with parts (c-e) showing the achieved resolution of 154, 100, 9 μm with silicon wafer thicknesses of 400, 110 and 6 μm achieving about $\lambda/45$ resolution. Recently Chen, et al. used an even thinner photomodulator, 180 nm thick vanadium dioxide, to obtain even better resolution at 4.5 *mu*m at $\lambda/100$ [57].

3.2.2 Electrical modulators

Electrical based modulators are likely to be the long-term future solution for spatial THz modulators because they have very little fundamental limitations. Namely, the maximum switch-rates are limited by the carrier recombination rates meaning they can potentially achieve megahertz switch rates, provided the RC constants of the devices are taken into account, especially with electrically tunable materials such as graphene [58, 59]. Their size is determined by photolithographic manufacturing technologies, which is already orders of magnitudes smaller than the THz wavelengths meaning that pixel sizes can be highly subwavelength. In fact, sometimes THz modulation structures can be too large for some commercial photolithographic systems. They are fully self-contained and compact, which is their main advantage over the optical based modulators (see §3.2.1) that need a laser, a spatial visible-light modulator and a photomodulator. However, in the near-term future they are unlikely to be commercially available. This is because their modulation amplitudes are determined by how carriers are injected/depleted via electrical gating and this is yet to optimized.

One of the first demonstrations of this modulation technique was by Kleine-Ostmann et al. in 2004 [60] where they electronically depleted carriers from a GaAs/AlGaAs interface, achieving about 3% modulation across a broadband frequency range of 0.1 to 2 THz. Since then there have been numerous attempts at improving the modulation depth, see references [61, 62] for recent reviews. These efforts have included enhancing the interaction between the THz wave and the charge carrier regions by metamaterial structures [63, 64]. Others have recently used graphene as the modulator [65, 66]. Using metamaterials or Fabry-Perot type resonances to enhance the modulation depth has the trade-off of reducing the working frequencies of the modulator. A further note is that subwavelength grating structures can enhance the THz modulation over a broadband range [58] for the correct THz polarization.

In 2014 C. M. Watts et al. created an electrical based THz-SLM in reference [67], and **Figure 4(a)** shows their experimental schematic and part (b) shows an image of their SLM. They electrically change the THz absorption of a 2 μm thick layer of n-doped GaAs, with each individual pixel being addressed by a FPGA array. The authors study the noise in final images from raster, random and Hadamard masks. Some of their results can be seen in **Figure 4(c)** and **(d)** with part (e) showing their object. Note, they were able to obtain 8×8 images at 1frames-per-second with **Figure 4(f)** showing 5 frames of the object in part (e) moving across the field of view. The device itself does not have large modulation depths meaning it mostly serves as a powerful proof-of-concept device. Another study creating an electrical based THz-SLM used graphene to create a 4×4 electro spatial-modulator [68]. And at last but certainly not least, we have the 2020 contribution of Y. Malevich et al. [69] where they built a 16×16 SLM by electrically gating two graphene layers

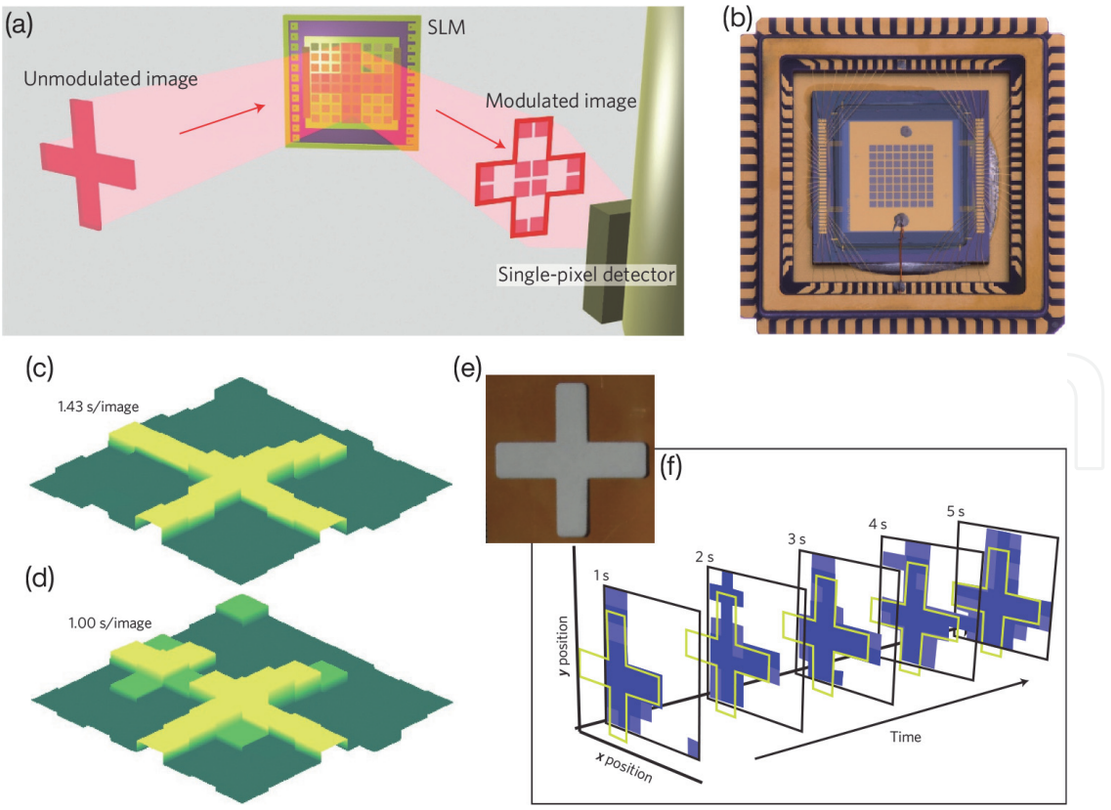

Figure 4.
(a) Schematic of the single-pixel imaging process utilizing an SLM. An image is spatially modulated by the metamaterial and the resulting radiation is sent to the single-pixel detector. (b) Photograph of the SLM (courtesy of K. burke, Boston College media technology services); total active area of the SLM is (4.8 mm²). (c) Image reconstruction using 64 masks with each mask displayed for 22.4 ms, giving a total image acquisition time of 1.43 s. (d) Image reconstruction using FISTA and 45 masks with each mask displayed for 22.4 ms, giving a total image acquisition time of 1 s. the colourmap scale of each reconstruction was chosen to best display the data. (e) Photograph of the object studied. The object was scanned across the field of view at a speed of 1.8 mm/s. (f) Consecutive tiles show FISTA reconstruction using 45 Hadamard masks. Only the first five frames are shown in the figure (see supplementary section 'compressive sensing' for full movie: 10 frames). The approximate position of the cross aperture is shown in yellow as a guide to the eye. Figure adapted from reference [67]. Copyright nature publishing group with re-use permission granted by Willie J. Padilla.

sandwiching an electrolyte. This device has broadband modulation depth and the electrolyte results in needing small voltages (below 4 V) meaning it can be easily integrated with microcontrollers. However the switch-rate, shown to be up-to 1 kHz, is limited by the generation of an electrical layer at the electrolyte-graphene interface, therefore more work is needed to optimize the modulation depth and switch rate. Nevertheless, these results [69] mark big progress towards a THz-SLM with a large number of pixels and low driving voltages.

3.3 Spatially patterned THz generation

Another innovative approach to single-pixel imaging is to create a spatially patterned beam at the generation step, rather than generate a homogeneous beam that is then spatially modulated, which has the benefit of not needing a THz-SLM. For the terahertz regime, this can be accomplished by three possible ways. First, having an array of photoconductive antennas [70–72], however this approach suffers from antenna cross-talk and inefficiency problems arising from the small working-area of the antennas whilst occupying a large area. Further, such antennas arrays have only been used as detectors. The second method is to use an electro-optic (EO) crystal that converts visible-light to THz frequencies via non-linear polarization effects [73]. The generation of THz radiation is localized to where the visible light is, hence projecting

a spatially varying light beam will generate a THz-beam with the same spatial features. This idea was implemented by references [74, 75] where they used a used a SLM to pattern an 800 nm femtosecond pulse and project that onto a ZnTe crystal. The third method is similar to the second one, with the difference being the use of a spintronic THz emitter instead of an electro-optic crystal. Here the inverse spin Hall effect is used to generate an ultrafast current transient that generates the THz radiation [76–78]. The spatial patterning is again done by a visible-light SLM since the THz generation is again localized to areas where the optical-pump was shined upon. This was demonstrated by Chen et al. in reference [79].

The similarities between the spintronic and electro-optic crystal approaches are that they both require femtosecond pulses with mJ/cm^2 powers and both measure the THz field-strength with sub-picosecond temporal resolution. The differences come from limitations imposed by the electro-optic crystals. First, absorption at the EO crystal phonons limits the working frequencies whereas spintronic emitters can emit from 1 to 30 THz [77], although organic EO crystals can significantly improve working bandwidth with commercial companies offering crystals emitting from 0.3 to 16 THz [80]. Second, EO crystals are typically thicker than the THz wavelengths for good working efficiency whereas spintronic emitters are nanometer thick allowing easier access to the THz near-fields for subwavelength resolution [79]. Finally, for the spintronic emitters the emitted THz polarization state is easily controlled by the externally applied magnetic field needed for THz emission [76], whereas for the EO crystal approach one needs to add an additional visible light SLM [81] resulting in increased system complexity.

Figure 5(a) shows the experimental setup of reference [79] which uses the spintronic emitter array approach. Note that the EO crystal approach is identical in that you only have to replace the spintronic emitter with the EO crystal and remove the magnetic field, then place the object as close as possible to the emitter array. One should note that the use of the second DMD in **Figure 5(a)** is only to correct the phase front induced by first DMD, which can also be achieved by the technique shown in the supplementary information of reference [82]. The spintronic emitter is nanometer thick hence Chen et al. was able to resolve metallic lines 6 μm in width, as shown in **Figure 5(c)–(g)**, which is significantly shorter than the THz wavelengths. Note, at these subwavelength scales polarization effects become significant as be seen when comparing **Figure 5(d)** and **(e)** where they show images with horizontal and vertical polarization, respectively, of the same object.

3.4 Liquid crystal THz modulators

Liquid crystal modulators work by the re-orientating the material molecules under an applied voltage. As the molecules are oblong, this changes the refractive index that an electro-magnetic wave experiences. Therefore these devices are great for phase modulation giving the greatest freedom in the values that the sampling matrix can take. In other words, they can theoretically project a Fourier matrix that has grayscale complex-values. Note that complex valued masks can be used in conjunction with an intensity only detector to obtain an image that has phase and amplitude information [83]. A liquid crystal based SLM for THz was computationally studied [84]. However, the re-orientation of the molecules is a slow process, and in the visible light regime liquid crystal displays are typically limited to below 100 Hz switch rates. Due to the longer THz wavelengths, thicker layers of liquid crystals are needed resulting in even slower switch rates. For this reason, liquid crystal spatial modulators for THz radiation have been limited mostly to applications where slow switching speeds are acceptable such as dynamically controllable lenses [85, 86], absorption [87] or polarization control [88].

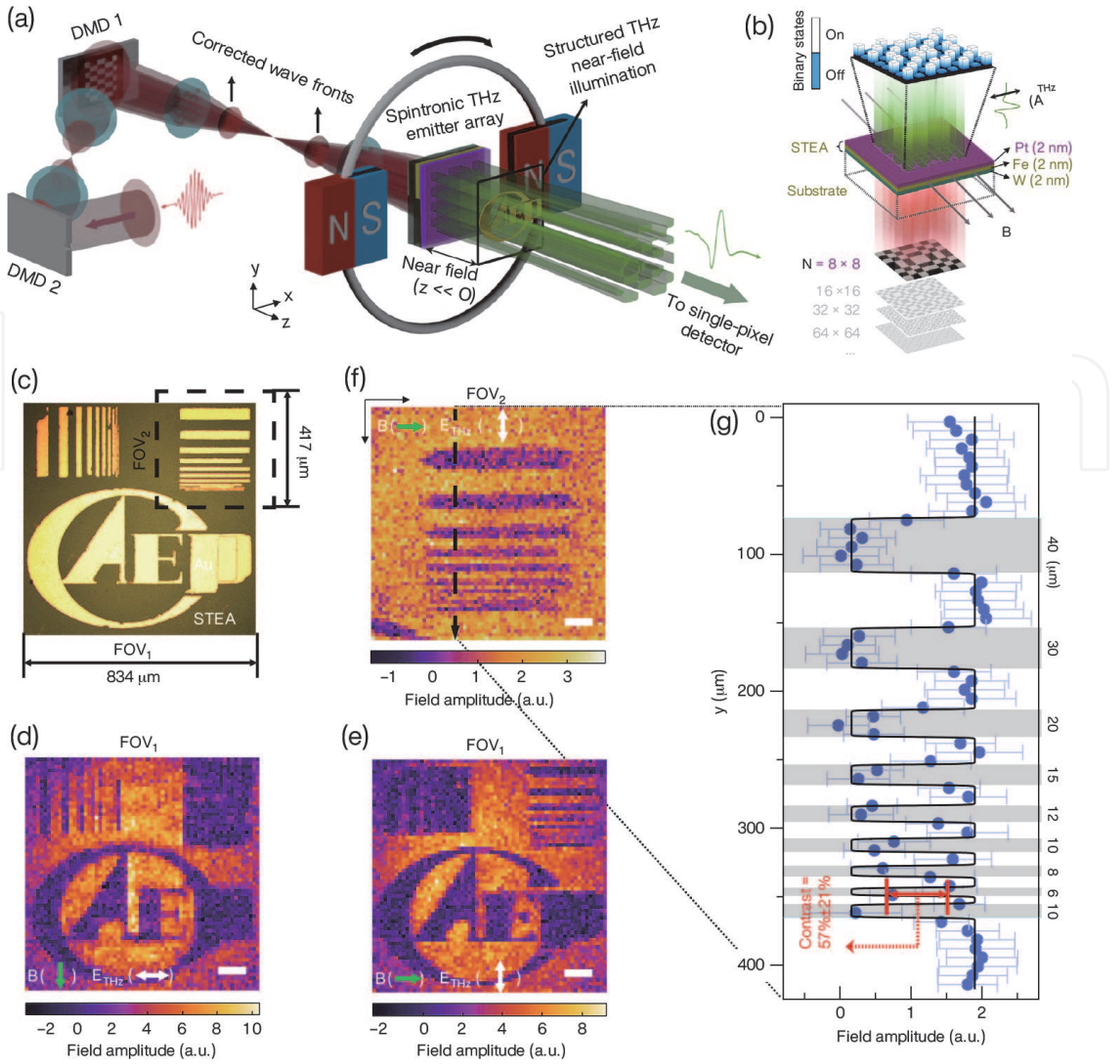

Figure 5.
(a) Schematic of the GHOSTEAM system. The spintronic THz emitter array (STEA) is excited by two-DMD-encoded fs laser pulses and generates spatially coded THz pulses. An object "CAEP" was placed in the near-field region ($z << \lambda$). The illuminating THz pulse was collected and sent to a single-pixel detector. (b) Schematic of the STEA, consisting of a W(2 nm)/Fe(2 nm)/Pt(2 nm) trilayer heterostructure and working in the binary emission state with polarization perpendicular to applied magnetic field. (c) Optical image of an object with a field of view of FOV 1 = 834 μm 834 *μm.* the bright regions are gold attached on the 150-nm-thick protective SiO_2 *layer on top of the STEA. THz ghost images in FOV 1 with a magnetic field (green arrows) applied along the vertical direction (d) and horizontal direction (e). The pixel size and scale bar are 13.0 μm* and 100 *μm, respectively, for both images. (f) THz ghost image in FOV 2 (indicated by the black dashed box in c) with a pixel size of 6.5 μm and a scale bar of 50 μm. the applied magnetic field B is along the horizontal direction (indicated by the green arrow), and the polarization of the THz radiation (indicated by the white double-headed arrow) is perpendicular to B. (g) Averaged amplitude of the THz field along the black dashed arrow in (f). Figure adapted and relabelled from reference [79]. Copyright nature publishing group with re-use permission under creative commons attribution 4.0 international license.*

4. Applications and discussion

The first demonstration of a single-pixel THz camera that uses a multi-pixel modulation approach[3] was in 2008 by Chan et al. [89]. Therein the authors showed amplitude and phase imaging was possible. Since Chan showed single-pixel THz imaging with metallic masks [89], most publications up until now have focused on

[3] Technically, a raster scanner is a single-pixel camera. However this chapter concerns itself when the beam of radiation has multiple scatters and apertures in each measurement. Therefore raster scanners are excluded.

improving the implementation by showing proof-of-concept modulation/generation techniques as opposed to potential applications. Shortly after in 2009 spectroscopic imaging was demonstrated [90]. The next experiment was in 2012 by Shen et al. [46] where they used a spinning disc with random masks, but it should be noted that their experiment used an infrared and a THz source whilst using the same SLM. The first demonstration of an optical based SLM was by Shrekenhamer et al. in 2013 [49]. The same group then published an electrical based SLM for single-pixel THz imaging in 2014 [67]. The next developments showed in 2016 that such imaging systems can detect a sub-wavelength fissure (8 μm) in a circuit board hidden by silicon [56]. Other applications show that these single-pixel cameras can be used for near-field biological imaging [91, 92], sub-wavelength THz mapping of graphene photoconductivity [82] as well as 2D tomographic imaging [93]. Further, observing hydration changes in a leaf due to intense light exposure over a 15 minute period has also been demonstrated [52]. Other recent studies include demonstrating a spinning disc system working from 3 to 13 THz using random masks [45]. Reference [94] shows how random, Hadamard and masks based on the discrete cosine transform perform in the THz regime and reference [95] studied Hadamard vs. Fourier masks in the context of undersampling performance.

The potential applications and capabilities of single-pixel THz cameras are directly determined by the THz source and detector, rather than the technique used to impart a spatial pattern in a beam of THz radiation. As such, it is unlikely for there to be a single-solution for all practical applications. Therefore, it is valuable to discuss where each of the techniques in §3 are likely to be used and how they compare to other THz imaging techniques. Metamaterial based SLMs, or specifically those that work over a few select frequencies, are unlikely to become widespread. This is because if you want to take an image only at one THz frequency then you can just use a bolometer detector array [18] and combine it with digital holography [19, 20] for an amplitude and phase measurement. Single-pixel imaging technologies are hampered by the serial data acquisition process, as such they will never truly compete at fast imaging rates with the parallel-data acquisition of detector arrays. As mentioned earlier, they compete in terms of being applicable when a detector array with the desired capabilities is just infeasible. This for THz technology translates itself to time-gated detection techniques that measure the amplitude and phase of a THz pulse with sub-picosecond temporal resolution, for example photo-conductive antennas [73].

The metallic/physical based masks, employed in §3.1, have contrast ratios of $\sim$ 99% over very large working frequencies. For example, holes in an aluminum plate could be used as an SLM for visible light as well for sub-THz frequencies and everything in between including ultrasound beams. The upper frequency limit is set by the plasma frequency whereas the lower frequency limit is set by the penetration depth at GHz frequencies. The major drawback is the physical movement involved in changing the masks. Using dynamically controlled mirrors, such those in **Figure 2**, requires no physical movement however their diffraction efficiency at low frequencies needs to be considered before implementation. Otherwise, their frequency response is going to be again to be determined by the reflection of a metal hence it is very broad. Such SLMs are probably most compatible for THz spectrometers that can measure between 1 and 30 THz [45], such as those based on air-plasma [96], spintronic [77] and organic EO crystals [80] emission techniques. This is of course compared to conductivity based SLMs of §3.2.

Modifying the Drude plasma frequency of a semiconductor via injection/depletion of charge carriers has great potential for compact integration of the entire imaging system, as long as electrical gating is used as it negates the need for an extra pump-laser. The drawback is that to ensure modulation depth over a large

frequency range the Drude plasma frequency has to be sufficiently modified. For example, after photoexcitation of silicon if ω_p moves from 0.01 THz to 25 THz, then the modulation depth for frequencies above 20 THz is going to be very poor. However, if the measurement only needs to measure frequencies between 0.1 and 2 THz with 100 fs temporal resolution, the working frequencies of many commercial THz-TDS systems, then this plasma frequency is going to be fine. For example, reference [52] achieved a 32×32 THz video with 6 frames-per-second using a system with such measurement capabilities. Their SLM is an optical excitation one, hence their system is not as compact as that shown in **Figure 4** but it demonstrates that fast THz imaging with single-pixel cameras is possible. Nevertheless, Chen et al. showed a THz amplitude modulation of near 200%[4] over the frequency range of 0.1 to 2 THz using electrical gating of graphene [59]. This shows electrical modulators have great potential but they are far from being commercially available as it was only in 2020 that a demonstration of 16×16 THz modulator was published [69], which has lower modulation depth and slower switch-rate than reference [52]. Finally, the physical resolution of these approaches is ultimately limited by the visible light pattern or the manufacturing technology used to make the array. As such, electrical modulators are capable of reaching resolutions of 150 nm and then not have issues of misalignment. In terms of sheer resolution, however, they are unlikely to compete with the 10 nm resolution achieved with AFM-tips [24] although due to the multiple scatterers and apertures in each measurement they will have larger SNRs [56] and thus offer quicker acquisition. A side note is that using Hadamard-Sylvester masks at sub-wavelength resolutions can result in grating-like diffraction effects for individual masks as shown in chapter 5.3.2 of reference [33].

Direct generation of a spatially varying THz beam, §3.3, has the benefit of not needing a THz-SLM at all, reducing the system complexity, whilst having visible light resolution. However, all the current techniques demonstrated have one major drawback: they need pulse energies around 1 mJ/cm^2 for sufficient signal-to-noise. A back of the envelope calculation shows that if such fluences are needed over a 500×500 μm square, then average laser powers of 2.5 mW, 0.625 W and 125 W incident onto the emitter area would be needed if the laser repetition rates are 1 kHz, 250 kHz and 50 MHz respectively[5]. The lower repetition rate lasers have lower signal-to-noise (measuring less pulses per unit time) and usually have larger laser noise-fluctuations causing further degradation. As such, these techniques are likely only usable for areas smaller than 500×500 μm where accessing the THz near-fields is necessary. Their competing technology is mapping out the THz fields onto a EO crystal using a CCD camera [21], which can achieve near-field resolution and still measure the THz-fields with sub-picosecond temporal resolution. Theoretically, neither the technique of reference [21] and that shown in **Figure 5** have an edge over of the other. However, in terms of experimental implementation the spintronic emitter array [79] has some advantages. Namely, easily controllable polarization and you need a high-quality camera for the EO-mapping approach [21] wheres as DMDs are low cost and found in everyday projectors. Finally, the EO-mapping approach needs an ultra-thin EO crystal thereby necessitating the use of an intense THz-source, whereas the spintronic array could possibly be implemented with a 100 kHz laser which should improve the SNR.

[4] This is was done by changing the reflection coefficient from 1 to -1 near the Brewster angle.

[5] Losses from various optical elements would occur and hence higher laser powers will be needed initially.

5. Conclusions

Although the first experimental implementations of single-pixel cameras can be traced back to 1976 [97], such imaging approaches were not widely studied or implemented in the commercial world. The reason is that the serial measurement of such ideas can not compete with parallel data acquisition of imaging arrays. Further, compressed sensing techniques began gaining mainstream attention in 2006 after two publications [37, 38]. This coincides with the development of visible light spatial modulators thereby allowing the implementation of the ideas in references [37, 38]. Whilst inherently slower than imaging arrays, these single-pixel cameras are much more robust and easier to implement in areas where imaging array technology is unavailable. In particular, the terahertz frequency regime.

This book chapter began by outlining the current state of THz cameras. Then it discusses the background theory of single-pixel imaging techniques. Most of the chapter was dedicated to discussing the current state of spatial THz-light modulators for use in single-pixel THz imaging in §3. The modulation techniques discussed are based on mechanical masks §3.1, optical §3.2.1 and electrical §3.2.2 modulation of conductivity, direct generation of spatially varying THz beams §3.3 and liquid crystal modulators §3.4. The final §4 is a discussion of the current state of single-pixel cameras as well the pros and cons of each different THz-SLM methodology.

The most advanced THz-SLM at present are those based on optical excitation of semiconductors, §3.2.1, however this is mostly because of their ease of implementation with current technology. Electrical modulators, §3.2.2, are likely to become the most used in the long term because compared to optical modulators they offer the same potential switch-speeds if not quicker, the same working frequencies, they are more compact and the physical resolution is limited by photolithrographic technology as opposed to visible light resolution. Further, the physical resolution been limited by the diffraction of the visible light-pump in an optical SLM is only achievable with high-power low-rep rate lasers, whereas electrical modulators would be compatible with fiber-based THz systems, that have magnitudes higher SNRs and are much cheaper, whilst maintaining the same resolution. Generating a THz beam with spatial variations has great resolution set by the visible-light diffraction limit, however their appeal will significantly drop the moment someone builds an electrical-based THz modulator with say 500×500 nm sized array elements that can be placed in the near-field of an object. Mechanical masks are mostly likely to be used in some niche applications that for example require simultaneous imaging with a THz beam and an ultrasonic beam. Liquid crystal modulators are unlikely to be used in single-pixel imaging unless there is a breakthrough that allows their switch-rates to reach 10 kHz, although they offer the most freedom in regards to the values of the projected masks (ie. complex grayscale values).

Ultimately, the development of single-pixel THz cameras is likely to proceed with optical modulators being used in university laboratories to optimize the algorithms and methodologies used in image recovery as well as synchronization of all the equipment. Simultaneously there will be an effort to develop electrical based array modulators that have fast-switch rates and large modulation depth over a broadband frequency range. Then the miniaturization of such modulator arrays will start and it is likely that at this point such commercially available THz-SLMs will become available from new specialized start-up companies. Spatially-generated THz beams will likely remain only in laboratories for fundamental studies of different systems, but are unlikely to be used for industrial and commercial applications mostly due to the requirement of pump powers of ~ 1 mJ/cm^2. Further, they are compatible with time-gated synchronization of visible-pump THz-probe

experiments allowing the study of sub-picosecond photoexcitation dynamics, hence their appeal to university labs.

Acknowledgements

This work was partially supported by the Research Grants Council of Hong Kong (project numbers 14206717 and 14201415), The Hong Kong Innovation and Technology Fund (project number ITS/371/16), The Engineering and Physical Sciences Research Council (grant number EP/S021442/1), and the Royal Society Wolfson Merit Award (EPM).

Conflict of interest

The authors declare no conflict of interest.

Nomenclature

AFM	Atomic force microscope
PCB	Printed Circuit Board
FPGA	Field-programmable gate array
SLM	Spatial light modulator
THz	Terahertz
EO	Electro-optic
SNR	Signa-to-noise ratio
DMD	Digital micromirror device
VO_2	Vanadium Dioxide
CCD	Charge Coupled device

Author details

Rayko Ivanov Stantchev[1] and Emma Pickwell-MacPherson[1,2*]

1 Department of Electronic Engineering, The Chinese University of Hong Kong, Hong Kong SAR

2 Physics Department, Warwick University, Coventry, UK

*Address all correspondence to: rayko@cuhk.edu.hk

References

[1] Mittleman, D. M. Twenty years of terahertz imaging [Invited]. *Optics Express* DOI: 10.1364/oe.26.009417 (2018).

[2] Chan, W. L., Deibel, J. & Mittleman, D. M. Imaging with terahertz radiation. *Reports on Progress in Physics* **70**, 1325–1379, DOI: 10.1088/0034-4885/70/8/R02 (2007).

[3] Jansen, C. *et al.* Terahertz imaging: applications and perspectives. *Applied Optics* 49, E48, DOI: 10.1364/AO.49.000E48 (2010).

[4] Dhillon, S. S. *et al.* The 2017 terahertz science and technology roadmap, DOI: 10.1088/1361-6463/50/4/043001 (2017).

[5] Dong, J. *et al.* Terahertz frequency-wavelet domain deconvolution for stratigraphic and subsurface investigation of art painting. *Optics Express* **24**, 26972–26985, DOI: 10.1364/OE.24.026972 (2016).

[6] Ahi, K., Asadizanjani, N., Shahbazmohamadi, S., Tehranipoor, M. & Anwar, M. Terahertz characterization of electronic components and comparison of terahertz imaging with x-ray imaging techniques. *SPIE* 94830K, DOI: 10.1117/12.2183128 (2015).

[7] Karpowicz, N. *et al.* Compact continuous-wave subterahertz system for inspection applications. *Applied Physics Letters* **86**, 054105, DOI: 10.1063/1.1856701 (2005).

[8] Dong, J. *et al.* Visualization of subsurface damage in woven carbon fiber-reinforced composites using polarization-sensitive terahertz imaging. *NDT and E International* DOI: 10.1016/j.ndteint.2018.07.001 (2018).

[9] Ulbricht, R., Hendry, E., Shan, J., Heinz, T. F. & Bonn, M. Carrier dynamics in semiconductors studied with time-resolved terahertz spectroscopy. *Reviews of Modern Physics* **83**, 543–586, DOI: 10.1103/RevModPhys.83.543 (2011).

[10] Shen, Y. C. Terahertz pulsed spectroscopy and imaging for pharmaceutical applications: A review. *International Journal of Pharmaceutics* **417**, 48–60, DOI: 10.1016/j.ijpharm.2011.01.012 (2011).

[11] Konek, C., Wilkinson, J., Esenturk, O., Heilweil, E. & Kemp, M. Terahertz spectroscopy of explosives and simulants: RDX, PETN, sugar, and L-tartaric acid. 73110K, DOI: 10.1117/12.817913 (International Society for Optics and Photonics, 2009).

[12] Kampfrath, T., Tanaka, K. & Nelson, K. A. Resonant and nonresonant control over matter and light by intense terahertz transients. *Nature Photonics* **7**, 680–690, DOI: 10.1038/nphoton.2013.184 (2013).

[13] Yu, C., Fan, S., Sun, Y. & Pickwell-MacPherson, E. The potential of terahertz imaging for cancer diagnosis: A review of investigations to date. *Quantitative Imaging in Medicine and Surgery* **2**, 33–45, DOI: 10.3978/j.issn.2223-4292.2012.01.04 (2012).

[14] Hernandez-Cardoso, G. G. *et al.* Terahertz imaging for early screening of diabetic foot syndrome: A proof of concept. *Scientific Reports* **7**, 1–9, DOI: 10.1038/srep42124 (2017).

[15] Titova, L. V. *et al.* Intense THz pulses cause H2AX phosphorylation and activate DNA damage response in human skin tissue. *Biomedical Optics Express* DOI: 10.1364/boe.4.000559 (2013).

[16] Escorcia, I., Grant, J., Gough, J. & Cumming, D. R. S. Uncooled CMOS terahertz imager using a metamaterial

absorber and pn diode. *Optics Letters* **41**, 3261–3264, DOI: 10.1364/ol.41.003261 (2016).

[17] Rogalski, A. & Sizov, F. Terahertz detectors and focal plane arrays. *Opto-Electronics Review* **19**, 346–404, DOI: 10.2478/s11772-011-0033-3 (2011).

[18] Amanti, M. I., Scalari, G., Beck, M. & Faist, J. Stand-alone system for high-resolution, real-time terahertz imaging. *Optics Express* **20**, 2772–2778, DOI: 10.1364/oe.20.002772 (2012).

[19] Locatelli, M. *et al.* Real-time terahertz digital holography with a quantum cascade laser. *Scientific Reports* **5**, 13566, DOI: 10.1038/srep13566 (2015).

[20] Yamagiwa, M. *et al.* Real-Time Amplitude and Phase Imaging of Optically Opaque Objects by Combining Full-Field Off-Axis Terahertz Digital Holography with Angular Spectrum Reconstruction. *Journal of Infrared, Millimeter, and Terahertz Waves* **39**, 561–572, DOI: 10.1007/s10762-018-0482-6 (2018).

[21] Blanchard, F. *et al.* Real-time terahertz near-field microscope. *Optics Express* **19**, 8277, DOI: 10.1364/OE.19.008277 (2011).

[22] Usami, M. *et al.* Development of a THz spectroscopic imaging system. *Physics in Medicine and Biology* **47**, 3749–3753, DOI: 10.1088/0031-9155/47/21/311 (2002).

[23] Huber, A. J., Keilmann, F., Wittborn, J., Aizpurua, J. & Hillenbrand, R. Terahertz near-field nanoscopy of mobile carriers in single semiconductor nanodevices. *Nano Letters* DOI: 10.1021/nl802086x (2008).

[24] Eisele, M. *et al.* Ultrafast multi-terahertz nano-spectroscopy with sub-cycle temporal resolution. *Nature Photonics* DOI: 10.1038/nphoton.2014.225 (2014).

[25] van der Valk, N. C. J. & Planken, P. C. M. Electro-optic detection of subwavelength terahertz spot sizes in the near field of a metal tip. *Applied Physics Letters* **81**, 1558, DOI: 10.1063/1.1503404 (2002).

[26] Macfaden, A. J., Reno, J. L., Brener, I. & Mitrofanov, O. 3 μm aperture probes for near-field terahertz transmission microscopy. *Applied Physics Letters* **104**, 011110, DOI: 10.1063/1.4861621 (2014).

[27] Chiu, C.-M. *et al.* All-terahertz fiber-scanning near-field microscopy. *Optics Letters* **34**, 1084, DOI: 10.1364/OL.34.001084 (2009).

[28] Hunsche, S., Koch, M., Brener, I. & Nuss, M. THz near-field imaging. *Optics Communications* **150**, 22–26, DOI: 10.1016/S0030-4018(98)00044-3 (1998).

[29] Zhao, J. *et al.* Terahertz imaging with sub-wavelength resolution by femtosecond laser filament in air. *Scientific Reports* DOI: 10.1038/srep03880 (2014).

[30] Gibson, G. M., Johnson, S. D. & Padgett, M. J. Single-pixel imaging 12 years on: a review. *Optics Express* **28**, 28190, DOI: 10.1364/OE.403195 (2020).

[31] Kutyniok, G. Theory and applications of compressed sensing. *GAMM-Mitteilungen* **36**, 79–101, DOI: 10.1002/gamm.201310005 (2013).

[32] Yates, F. Complex Experiments. *Supplement to the Journal of the Royal Statistical Society* **8**, 27–41, DOI: 10.2307/2983638 (1935).

[33] Stantchev, R. I. *Non-invasive near-field THz imaging using a single pixel detector*. Ph.D. thesis, University of Exeter (2017).

[34] Zhang, Z., Wang, X., Zheng, G. & Zhong, J. Hadamard single-pixel

imaging versus Fourier single-pixel imaging. *Optics Express* DOI: 10.1364/oe.25.019619 (2017).

[35] Harwit, M. & Sloane, N. J. A. *Hadamard Transform Optics* (Academic Press, New York, 1979).

[36] Paley, R. E. A. C. On orthogonal matrices. *J. Math. Phys* **12**, 311–320 (1933).

[37] Candes, E., Romberg, J. & Tao, T. Robust uncertainty principles: exact signal reconstruction from highly incomplete frequency information. *IEEE Transactions on Information Theory* **52**, 489–509, DOI: 10.1109/TIT.2005.862083 (2006).

[38] Donoho, D. L. Compressed sensing. *IEEE Transactions on Information Theory* **52**, 1289–1306, DOI: Doi10.1109/Tit.2006.871582 (2006).

[39] Candes, E. & Romberg, J. l1-magic: Recovery of sparse signals via convex programming, https://github.com/scgt/l1magic (2005).

[40] Li, C., Yin, W., Jiang, H. & Zhang, Y. An efficient augmented Lagrangian method with applications to total variation minimization. *Computational Optimization and Applications* DOI: 10.1007/s10589-013-9576-1 (2013).

[41] Li, C., Yin, W. & Yin, Z. TVAL3: TV minimization by Augmented Lagrangian and ALternating direction ALgorithms, https://www.caam.rice.edu/∼optimization/L1/TVAL3/ (2010).

[42] Czajkowski, K. M., Pastuszczak, A. & Kotyński, R. Real-time single-pixel video imaging with Fourier domain regularization. *Optics Express* **26**, 20009, DOI: 10.1364/OE.26.020009 (2018).

[43] Czajkowski, K. M., Pastuszczak, A. & Kotyński, R. FDRI single-pixel imaging, h ttps://github.com/KMCzajkowski/ FDRI-single-pixel-imaging (2020).

[44] Giles, R. H. Characterization of Material Properties at Terahertz Frequencies. *Submillimeter Technology Laboratory, University of Massachusetts* (1995).

[45] Vallés, A., Jiahuan, H. E., Ohno, S., Omatsu, T. & Miyamoto, K. Broadband high-resolution terahertz single-pixel imaging. *arXiv* DOI: 10.1364/oe.404143 (2020).

[46] Shen, H. *et al.* Spinning disk for compressive imaging. *Optics Letters* DOI: 10.1364/ol.37.000046 (2012).

[47] Kappa, J. *et al.* Electrically Reconfigurable Micromirror Array for Direct Spatial Light Modulation of Terahertz Waves over a Bandwidth Wider Than 1 THz. *Scientific Reports* DOI: 10.1038/s41598-019-39152-y (2019).

[48] Alius, H. & Dodel, G. Amplitude-, phase-, and frequency modulation of far-infrared radiation by optical excitation of silicon. *Infrared Physics* 32, 1–11, DOI: 10.1016/0020-0891(91)90090-3 (1991).

[49] Shrekenhamer, D., Watts, C. M. & Padilla, W. J. Terahertz single pixel imaging with an optically controlled dynamic spatial light modulator. *Optics Express* **21**, 12507, DOI: 10.1364/OE.21.012507 (2013).

[50] Cavalleri, A. *et al.* Femtosecond structural dynamics in VO2 during an ultrafast solid-solid phase transition. *Physical Review Letters* DOI: 10.1103/physrevlett.87.237401 (2001).

[51] Jeong, J. *et al.* Suppression of metal-insulator transition in VO2 by electric field-induced oxygen vacancy formation. *Science* DOI: 10.1126/science.1230512 (2013).

[52] Stantchev, R. I., Yu, X., Blu, T. & Pickwell-MacPherson, E. Real-time terahertz imaging with a single-pixel

detector. *Nature Communications* DOI: 10.1038/s41467-020-16370-x (2020).

[53] Stantchev, R. I. *et al.* Compressed sensing with near-field THz radiation. *Optica* DOI: 10.1364/optica.4.000989 (2017).

[54] Hooper, I. R. *et al.* High efficiency photomodulators for millimeter wave and THz radiation. *Scientific Reports* DOI: 10.1038/s41598-019-54011-6 (2019).

[55] Kannegulla, A., Shams, M. I. B., Liu, L. & Cheng, L.-J. Photo-induced spatial modulation of THz waves: opportunities and limitations. *Optics Express* DOI: 10.1364/oe.23.032098 (2015).

[56] Stantchev, R. I. *et al.* Noninvasive, near-field terahertz imaging of hidden objects using a single-pixel detector. *Science Advances* 2, e1600190 (2016).

[57] Chen, S.-C. *et al.* Terahertz wave near-field compressive imaging with a spatial resolution of over $\lambda/100$. *Optics Letters* DOI: 10.1364/ol.44.000021 (2019).

[58] Sun, Y. *et al.* Graphene-loaded metal wire grating for deep and broadband THz modulation in total internal reflection geometry. *Photonics Research* DOI: 10.1364/prj.6.001151 (2018).

[59] Chen, Z. *et al.* Graphene controlled Brewster angle device for ultra broadband terahertz modulation. *Nature Communications* DOI: 10.1038/s41467-018-07367-8 (2018).

[60] Kleine-Ostmann, T., Dawson, P., Pierz, K., Hein, G. & Koch, M. Room-temperature operation of an electrically driven terahertz modulator. *Applied Physics Letters* DOI: 10.1063/1.1723689 (2004).

[61] Degl'Innocenti, R., Kindness, S. J., Beere, H. E. & Ritchie, D. A. All-integrated terahertz modulators. *Nanophotonics* DOI: 10.1515/nanoph-2017-0040 (2018).

[62] Wang, L. *et al.* A review of THz modulators with dynamic tunable metasurfaces. *Nanomaterials* DOI: 10.3390/nano9070965 (2019).

[63] Chen, H. T. *et al.* Active terahertz metamaterial devices. *Nature* DOI: 10.1038/nature05343 (2006).

[64] Chen, H. T. *et al.* A metamaterial solid-state terahertz phase modulator. *Nature Photonics* DOI: 10.1038/nphoton.2009.3 (2009).

[65] Lee, S. H. *et al.* Switching terahertz waves with gate-controlled active graphene metamaterials. *Nature Materials* DOI: 10.1038/nmat3433 (2012).

[66] Sensale-Rodriguez, B. *et al.* Extraordinary control of terahertz beam reflectance in graphene electro-absorption modulators. *Nano Letters* DOI: 10.1021/nl3016329 (2012).

[67] Watts, C. M. *et al.* Terahertz compressive imaging with metamaterial spatial light modulators. *Nat. Photon.* **8**, 605–609, DOI: 10.1038/nphoton.2014.139 (2014).

[68] Sensale-Rodriguez, B. *et al.* Terahertz imaging employing graphene modulator arrays. *Optics Express* DOI: 10.1364/oe.21.002324 (2013).

[69] Malevich, Y., Ergoktas, S., M., Bakan, G., Steiner, P. & Kocabas, C. Video-Speed Graphene Modulator Arrays for Terahertz Imaging Applications. *ACS Photonics* **7**, 2374–2380, DOI: 10.1021/acsphotonics.0c00991 (2020).

[70] Nallappan, K. *et al.* A dynamically reconfigurable terahertz array antenna for 2D-imaging applications. In *2017 Photonics North, PN 2017,* DOI: 10.1109/PN.2017.8090603 (2017).

[71] Pradarutti, B. *et al.* Terahertz line detection by a microlens array coupled photoconductive antenna array. *Optics Express* DOI: 10.1364/oe.16.018443 (2008).

[72] Brahm, A. *et al.* Multichannel terahertz time-domain spectroscopy system at 1030 nm excitation wavelength. *Optics Express* DOI: 10.1364/oe.22.012982 (2014).

[73] Reimann, K. Table-top sources of ultrashort THz pulses. *Reports on Progress in Physics* DOI: 10.1088/0034-4885/70/10/R02 (2007).

[74] Olivieri, L. *et al.* Hyperspectral terahertz microscopy via nonlinear ghost imaging. *Optica* 7, 186–191, DOI: 10.1364/OPTICA.381035 (2020).

[75] Zhao, J., Yiwen, E., Williams, K., Zhang, X. C. & Boyd, R. W. Spatial sampling of terahertz fields with sub-wavelength accuracy via probe-beam encoding. *Light: Science and Applications* DOI: 10.1038/s41377-019-0166-6 (2019).

[76] Kong, D. *et al.* Broadband Spintronic Terahertz Emitter with Magnetic-Field Manipulated Polarizations. *Advanced Optical Materials* DOI: 10.1002/adom.201900487 (2019).

[77] Seifert, T. *et al.* Efficient metallic spintronic emitters of ultrabroadband terahertz radiation. *Nature Photonics* DOI: 10.1038/nphoton.2016.91 (2016).

[78] Kampfrath, T. *et al.* Terahertz spin current pulses controlled by magnetic heterostructures. *Nature Nanotechnology* DOI: 10.1038/nnano.2013.43 (2013).

[79] Chen, S. C. *et al.* Ghost spintronic THz-emitter-array microscope. *Light: Science and Applications* DOI: 10.1038/s41377-020-0338-4 (2020).

[80] Photonics, R. Terahertz Generators and Detectors: Electro-Optic DSTMS Crystals, http://rainbowphotonics.com/prod_dstms.php.

[81] Sato, M. *et al.* Terahertz polarization pulse shaping with arbitrary field control. *Nature Photonics* DOI: 10.1038/nphoton.2013.213 (2013).

[82] Hornett, S. M., Stantchev, R. I., Vardaki, M. Z., Beckerleg, C. & Hendry, E. Subwavelength Terahertz Imaging of Graphene Photoconductivity. *Nano Letters* DOI: 10.1021/acs.nanolett.6b03168 (2016).

[83] Saqueb, S. A. N. & Sertel, K. Phase-Sensitive Single-Pixel THz Imaging Using Intensity-Only Measurements. *IEEE Transactions on Terahertz Science and Technology* DOI: 10.1109/TTHZ.2016.2610760 (2016).

[84] Savo, S., Shrekenhamer, D. & Padilla, W. J. Liquid crystal metamaterial absorber spatial light modulator for THz applications. *Advanced Optical Materials* DOI: 10.1002/adom.201300384 (2014).

[85] Zhou, S. *et al.* Liquid crystal integrated metalens with dynamic focusing property. *Optics Letters* DOI: 10.1364/ol.398601 (2020).

[86] Shen, Z. *et al.* Liquid crystal tunable terahertz lens with spin-selected focusing property. *Optics Express* DOI: 10.1364/oe.27.008800 (2019).

[87] Shrekenhamer, D., Chen, W. C. & Padilla, W. J. Liquid crystal tunable metamaterial absorber. *Physical Review Letters* DOI: 10.1103/PhysRevLett.110.177403 (2013).

[88] Chen, X. *et al.* Highly Efficient Ultra-Broadband Terahertz Modulation Using Bidirectional Switching of Liquid Crystals. *Advanced Optical Materials* DOI: 10.1002/adom.201901321 (2019).

[89] Chan, W. L. *et al.* A single-pixel terahertz imaging system based on

compressed sensing. *Applied Physics Letters* **93**, 121105, DOI: 10.1063/1.2989126 (2008).

[90] Shen, Y. C. *et al.* Terahertz pulsed spectroscopic imaging using optimized binary masks. *Applied Physics Letters* DOI: 10.1063/1.3271030 (2009).

[91] Stantchev, R. I. *et al.* Subwavelength hyperspectral THz studies of articular cartilage. *Scientific Reports* DOI: 10.1038/s41598-018-25057-9 (2018).

[92] Barr, L. E. *et al.* Total internal reflection based super-resolution imaging for sub-IR frequencies. *arXiv preprint: 2006.02091* (2020).

[93] Mohr, T., Herdt, A. & Elsässer, W. 2D tomographic terahertz imaging using a single pixel detector. *Optics Express* DOI: 10.1364/oe.26.003353 (2018).

[94] Augustin, S., Frohmann, S., Jung, P. & Hübers, H. W. Mask responses for single-pixel terahertz imaging. *Scientific Reports* DOI: 10.1038/s41598-018-23313-6 (2018).

[95] She, R., Liu, W., Lu, Y., Zhou, Z. & Li, G. Fourier single-pixel imaging in the terahertz regime. *Applied Physics Letters* DOI: 10.1063/1.5094728 (2019).

[96] Clough, B., Dai, J. & Zhang, X. C. Laser air photonics: Beyond the terahertz gap, DOI: 10.1016/S1369-7021(12)70020-2 (2012).

[97] Sloane, N. J. A. & Harwit, M. Masks for Hadamard transform optics, and weighing designs. *Applied Optics* DOI: 10.1364/ao.15.000107 (1976).